Volume 19, Number 2, 2026. pp. 201-212

Jordan Journal of Physics

ARTICLE

The Impact of pH Value on the Structural, Optical, and Magnetic Characteristics of Nickel Ferrite Nanoparticles Produced Hydrothermally for Use in Photodetectors

Nabeel W. Mamdooh[a], **Saeed N. T. AlRashid**[a], and **Isam M. Ibrahim**[b]

[a] *Department of Physics, College of Education for Pure Science, University of Anbar, Ramady, Iraq.*

[b] *Department of Physics, College of Science, University of Baghdad, Baghdad, Iraq.*

DOI: **https://doi.org/10.47011/19.2.7**

Received on: 16/12/2024; *Accepted on: 07/05/2025*

Abstract: This study investigates the synthesis of nickel ferrite nanoparticles ($NiFe_2O_4$) using the hydrothermal method at different pH values (5, 9, and 11). The synthesized nanoparticles were characterized using X-ray diffraction (XRD), field emission scanning electron microscopy (FESEM), energy dispersive X-ray (EDX), UV-Vis spectroscopy, and a vibrating sample magnetometer (VSM). XRD analysis confirmed the crystalline nature of $NiFe_2O_4$ with a face-centered cubic (FCC) structure. FESEM images revealed the formation of spherical nanoparticles with sizes below 100 nm, while EDX analysis verified the presence of nickel and iron elements.

Magnetic characterization using VSM demonstrated the magnetic behavior of the synthesized nanoparticles through parameters such as saturation magnetism (Ms) and coercivity (H_c). The saturation magnetization increased with increasing pH, with values of 5, 9, and 11, respectively. UV-Vis spectroscopy exhibited a blue shift in the surface plasmon resonance (SPR) absorption peak with increasing pH. Optical analysis indicated that the optical band gap energy increased from 3.35 to 4.01 eV as the pH increased from 5 to 11, following a direct electronic transition.

Based on the structural, optical, and magnetic analyses, pH11 was identified as the optimal condition for synthesizing nickel ferrite nanoparticles and was subsequently employed in photodetector applications. The fabricated photodetector exhibited a high photosensitivity of 231.89% and demonstrated a rapid and significant photoresponse under illumination at 350 nm.

Keywords: Magnetic properties, Nickel ferrite, Hysteresis, Hydrothermal, Photodetector.

1. Introduction

Nanotechnology has witnessed remarkable advances over the past few decades, particularly in the field of physical sciences. It is generally defined as the manipulation and control of materials with a high degree of precision at the nanoscale, including their size, structure, and functional properties. At this scale, materials exhibit unique physical and chemical characteristics that differ significantly from those observed in their bulk form. These distinctive properties arise primarily from the substantial increase in surface area-to-volume ratio as well as quantum confinement effects [1, 2]. Ferrite nanoparticles have attracted considerable attention due to their remarkable magnetic properties and their wide range of technological applications, including environmental remediation, magnetic recording devices, sensors, inductors, switching circuits, ferrofluids, soft magnetic cores, communication systems, and water purification technologies. Spinel ferrites generally possess the chemical formula MFe_2O_4, where M^{2+} represents a divalent metal ion such as Ni, Zn, Co, Mg, Cu, Mn.

Corresponding Author: Nabeel W. Mamdooh **Email**: nbeelwleed@gmail.com

In the cubic spinel structure, small Fe^{3+} and M^{2+} ions occupy the tetrahedral (A) and octahedral [B] interstitial sites within the crystal lattice. Based on the distribution of metal ions between the (A) and [B] sites, spinel ferrites are commonly classified into three categories. Divalent M^{2+} ions occupy tetrahedral sites and Fe^{3+} ions occupy octahedral sites in the first class, known as normal spinel. In the second class, known as inverse spinel, Fe^{3+} ions are equally distributed between tetrahedral and octahedral sites, while divalent M^{2+} ions occupy octahedral sites. The degree of inversion in a spinel structure is determined by the fraction of divalent M^{2+} ions occupying the octahedral [B] sites in mixed spinels, which represent the third category of spinel ferrites. The distribution of divalent M^{2+} ions within the spinel lattice significantly influences the magnetic properties of the material, making spinel ferrites suitable for a wide range of technological applications.

Among these materials, nickel ferrite ($NiFe_2O_4$) is classified as an inverse spinel ferrite and is characterized by soft magnetic behavior and moderate saturation magnetization [3, 4]. Nickel ferrite is a soft, versatile ferrite material with low conductivity and good electrochemical stability. It is also found in abundance in nature, making it suitable for use in numerous industrial and technological applications, such as storing high-density magnetic information, improving magnetic resonance imaging (MRI), light sensing, gas sensors, magnetic fluids, magnetic storage systems, drug delivery, photovoltaic materials, microwave devices, etc. [5]. It is known for its ferromagnetic properties and has the highest magnetic density. In addition, nanoscale nickel ferrites are unique in many properties with modified applications, such as high-frequency applications, biomedical applications, environmental remediation applications, and low-loss electronic devices [6]. Additionally, nickel spinels offer a number of benefits, including affordability, photochemical stability, and a good response to visible light. As a result, they can be applied to photooxidation, solar cells, and photodetector applications [7]. Numerous chemical and physical methods have been employed for the synthesis of nickel ferrite nanoparticles, including co-precipitation, spray pyrolysis, solid-state reactions, thermal decomposition, high-temperature self-propagation, hydrothermal techniques, microemulsion methods, mechanical synthesis, sol-gel processes, and combustion techniques [8]. The hydrothermal method is one of the most widely used techniques due to its simplicity and high degree of composition control. Furthermore, hydrothermal synthesis does not need complicated or extremely high processing temperatures. For instance, the solid-state method can produce nickel ferrite at 800 °C, whereas the hydrothermal method needs a temperature of approximately 150 °C [9, 10]. A crucial factor in regulating the characteristics of ferrite is adjusting the pH level during the chemical reaction. This pH level adjustment has been demonstrated to have a major impact on the semiconductor characteristics of nano-sized $NiFeO_2$ ferrite [11].

This study used a hydrothermal method to synthesize nanosized nickel ferrite ($NiFe_2O_4$) at various pH levels. It was noted how pH affected the structural, magnetic, and optical characteristics. The evaluation results were presented using a vibrating sample magnetometer (VSM), energy dispersive X-ray (EDX), X-ray diffraction (XRD), field emission scanning electron microscopy (FESEM), and UV-visible spectroscopy. It was employed in photosensor applications after the ideal pH value was determined based on structural, optical, and magnetic characteristics.

2. Experimental Method

2.1 Material

The Merck Chemical Company was the source of $NiSO_4.6H_2O$, $FeSO_4.7H_2O$, and NaOH, which were used straight out of the container without further purification. All of the experiments used deionized water, which had a conductivity of less than 10^{-6} Scm^{-1}.

2.2 Synthesis of Nickel Ferrite Nanoparticles

A 0.1 M (50 mL) solution of ferrous sulfate ($FeSO_4.7H_2O$) was mixed with a 0.1 M (25 mL) solution of nickel sulfate ($NiSO_4.6H_2O$) in twice-distilled deionized water under vigorous stirring. Sodium hydroxide (NaOH) was added to the sample to control the pH at different pH levels (5, 9, and 11 pH). Following preparation, the sample was put in an autoclave reactor and heated to 150 °C for three hours to undergo hydrothermal synthesis. The prepared material was put into a centrifuge and thoroughly cleaned with ethanol and deionized water. The material was dried for three hours at 50 °C in an oven.

Characterization analyses were performed on the synthesized powder samples. After determining the optimal pH condition through structural, optical, and magnetic characterization, the selected sample was utilized in a photosensor application following its deposition onto n-type silicon.

2.3 Characterization of $NiFe_2O_4$ Nanoparticles

The morphological, optical, structural, magnetic, and compositional properties of nickel ferrite nanoparticles ($NiFe_2O_4$) were calculated by means of field emission scanning electron microscopy (FE-SEM), X-ray diffraction (XRD), energy dispersive X-ray spectroscopy (EDS), vibration sample magnetometer (VSM), and ultraviolet-visible (UV-Vis).

Results and Discussion

3.1 X-ray Diffraction Analysis

The X-ray diffraction (XRD) technique was used to study the crystal structure properties and to investigate the identity of the compound, phase, and lattice parameters. Figure 1 shows the XRD patterns of the synthesized nickel ferrite nanoparticles prepared at different pH values (5, 9, and 11) in order to investigate the effect of pH variation on the crystallization behavior of the nanoparticles. The diffraction patterns in Fig. 1 show a face-centered cubic (FCC) crystal structure for the $NiFe_2O_4$ nanoparticles. It can be observed that most of the diffraction peaks in the 2θ angular range from 30º to 65º, and the "hkl" values were compared with the standard JCPDS file with the numbered card (PCPDF 86-2267). In addition, weak peaks corresponding to an unidentified impurity phase were observed. Using standard data, it was observed that the XRD peaks marked (220), (311), (400), (422), (511), and (440) are consistent with the FCC fluorite structure of nickel ferrite. The sharp peaks indicate a high degree of crystallinity, and the peak (311) represents the dominant reflection of $NiFe_2O_4$, which is consistent with the results of previous studies [12-14].

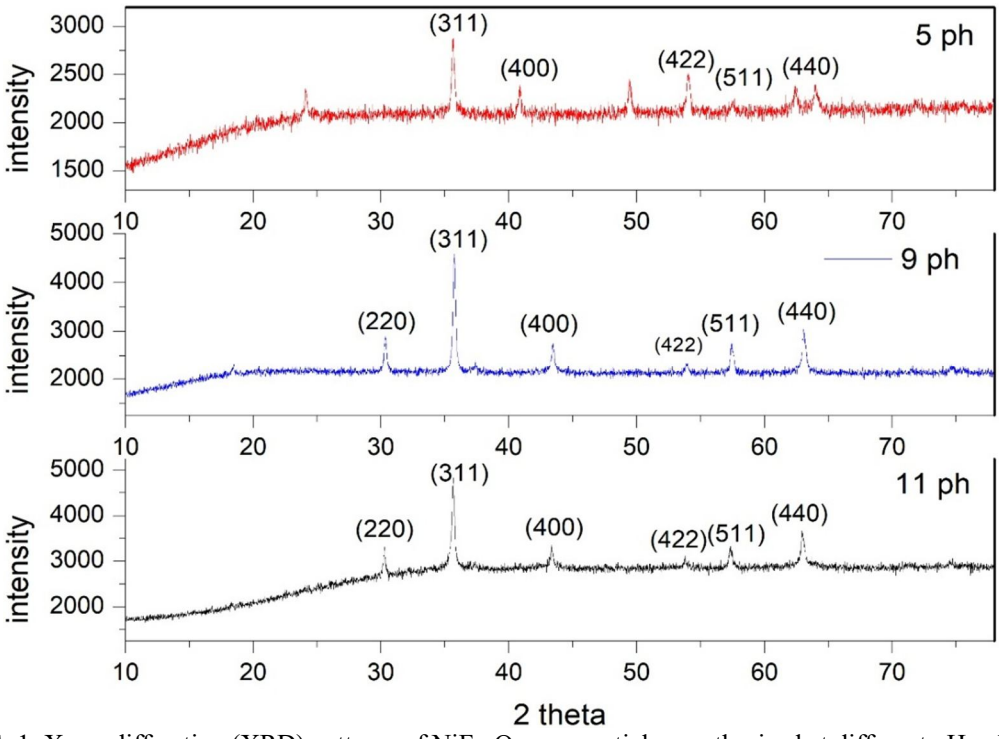

FIG. 1. X-ray diffraction (XRD) patterns of $NiFe_2O_4$ nanoparticles synthesized at different pH values.

The XRD patterns shown in Fig. 1 confirm the successful synthesis of $NiFe_2O_4$ nanoparticles and demonstrate the influence of pH on their crystal structure and crystallite size distribution. An increase in pH results in higher diffraction peak intensities, indicating an improvement in the crystallinity of the synthesized nanoparticles

This is in line with previous studies reporting that variations in pH during the synthesis process can induce structural and crystallographic modifications associated with nucleation and

crystal growth processes during heat treatment [15, 16].

Table 1 displays the values of the crystal size (D) of $NiFe_2O_4$ nanoparticles estimated using the Debye-Scherrer Eq. (1): the distance (d) between crystal planes, the surface area (S.A) (2), the dislocation density (δ) (3), and the microstrain (ε) (4).

The following formulas were used to determine the crystal parameters [17]:

$$D = \frac{k\lambda}{\beta \cos\theta} \quad (1)$$

$$\mathrm{S.A} = \frac{6}{D\rho} \quad (2)$$

$$\delta = \frac{1}{\mathrm{D}^2}\,. \quad (3)$$

$$\varepsilon = \frac{\beta_{1/2}}{4\tan\theta}\,. \quad (4)$$

TABLE 1. The microstructural characteristics and crystal size of $NiFe_2O_4$ formed at different pH values.

Temp	2θ	d-spacing [Å]	FWHM Left [°2θ]	Plan (hkl)	Crystallite Size(D) (nm)	Surface area (S.A) × $10^3 cm^2/g$	*Dislocation density* *(δ)* × 10^{11} / cm^2	Micro Strain only [%]
5 PH	35.6129	2.51894	0.2227	(311)	37.5	180	0.71	0.37594
	40.8191	2.0888	0.2327	(400)	36.4	185	0.75	0.24886
	54.0018	1.69668	0.2472	(422)	36	187	0.77	0.20602
	57.3401	1.806	0.2661	(511)	43.3	156	0.53	0.19846
	62.3907	1.48719	0.2551	(440)	36.4	185	0.75	0.18948
9 PH	30.3169	2.94582	0.2191	(220)	37.6	179	0.71	0.39337
	35.7114	2.51222	0.2358	(311)	35.4	190	0.8	0.35081
	43.4046	2.08311	0.2327	(400)	36.7	184	0.74	0.34485
	53.873	1.70043	0.2597	(422)	34.3	196	0.85	0.22344
	57.4083	1.60383	0.224	(511)	40.4	167	0.61	0.18615
	63.0488	1.47324	0.2334	(440)	39.9	169	0.63	0.2232
11 PH	30.2425	2.9529	0.3133	(220)	26.3	256	1.44	0.8605
	35.6204	2.51843	0.2463	(311)	33.9	198	0.87	0.52197
	43.3166	2.08713	0.2907	(400)	29.4	229	1.15	0.52225
	53.7544	1.7039	0.236	(422)	37.7	179	0.7	0.00272
	57.3082	1.60639	0.2026	(511)	44.7	151	0.5	0.15877
	62.9433	1.47545	0.229	(440)	40.7	165	0.6	0.17709

The data in Table 1 shows that the crystal size changes slightly when the pH is raised from 5 to 11. We note that the crystal size resulting from the main reflection (311) for the three samples ranges from 37.5 to 33.9 nm. This is due to the fact that pH plays a controlling role in crystal formation and growth during the synthesis process [18]. It is also observed that the values of dislocation density (δ), surface area (S.A.), and microstress (ε) increase with increasing pH due to the decrease in crystal size. Among the prepared samples, sample 11 had the highest degree of crystallinity and the largest surface area, as shown in the Table.

3.2 Results of Scanning Electron Microscopy (FESEM) Examinations

The morphology (shape, size, and distribution) of nickel ferrite particles made by the hydrothermal process at various pH levels is depicted in Fig. 2, as obtained through FESEM images.

This analysis demonstrates that increasing the pH leads to a more uniform and regular morphology and distribution of $NiFe_2O_4$ nanoparticles, providing strong evidence that pH plays a significant role in determining the properties of nanomaterials [19].

The presence of nickel ferrite nanoparticles is clearly visible in Fig. 2. They are mostly spherical in shape with particle sizes below 100 nm confirming their nanoscale dimensions. In addition to the spherical morphology, some irregularly shaped agglomerates are observed. These agglomerations may arise during the cooling process or as a result of the magnetic nature of the nanoparticles, as well as weak interparticle interactions such as van der Waals forces, which promote particle clustering [20].

3.3 Energy Dispersive X-ray Spectroscopy (EDX)

An analytical method for determining the compositions of different elements in a sample is energy-dispersive X-ray spectroscopy (EDS, EDX, EDXS, or XEDS), also known as energy-dispersive X-ray analysis (EDXA) or energy-dispersive X-ray microscopy (EDXMA). It depends on how the sample and specific X-ray excitation sources interact [21]. The findings of a quantitative and qualitative examination of nickel ferrite nanoparticles made using the hydrothermal method at various pH levels are displayed in Fig. 3. From the Figure, we notice the presence of iron and nickel as constituent elements, as well as the increase in the percentage of oxygen with increasing pH [19, 20]. The EDX figure confirms the agreement with the XRD results, which revealed the presence of impurity phases in the first sample and the detection of a single ferrite phase in the other two samples.

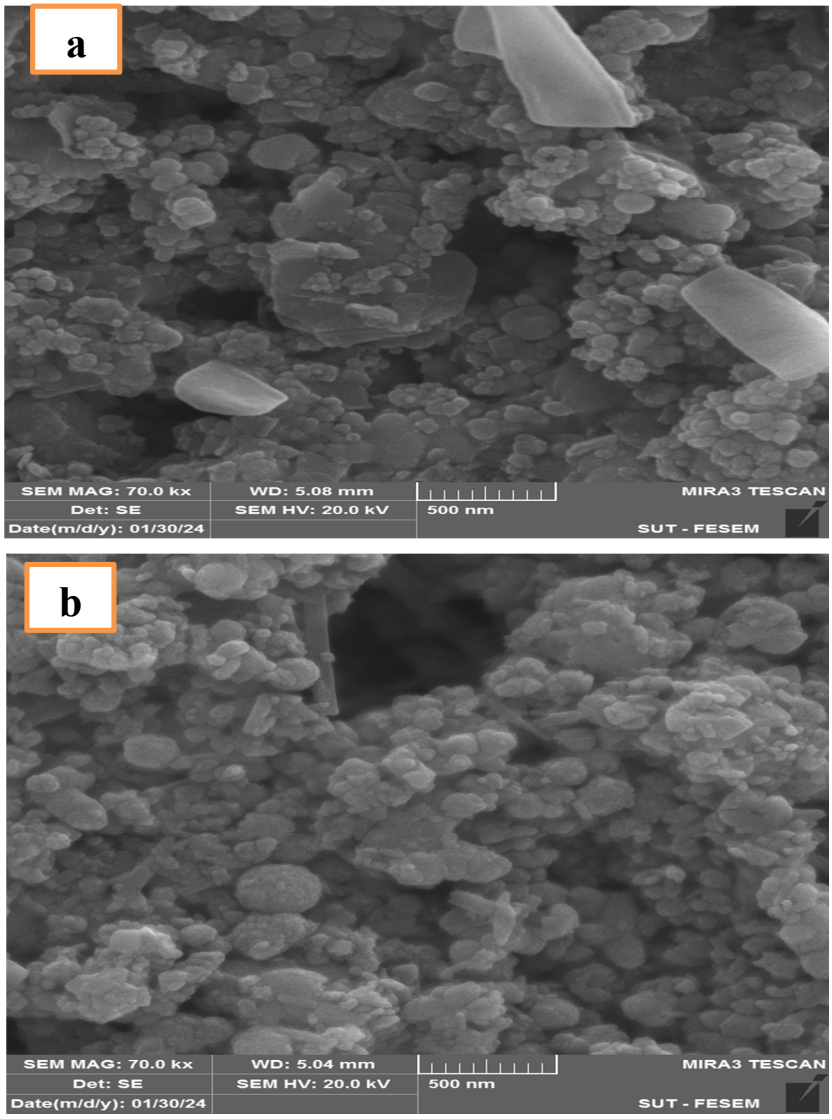

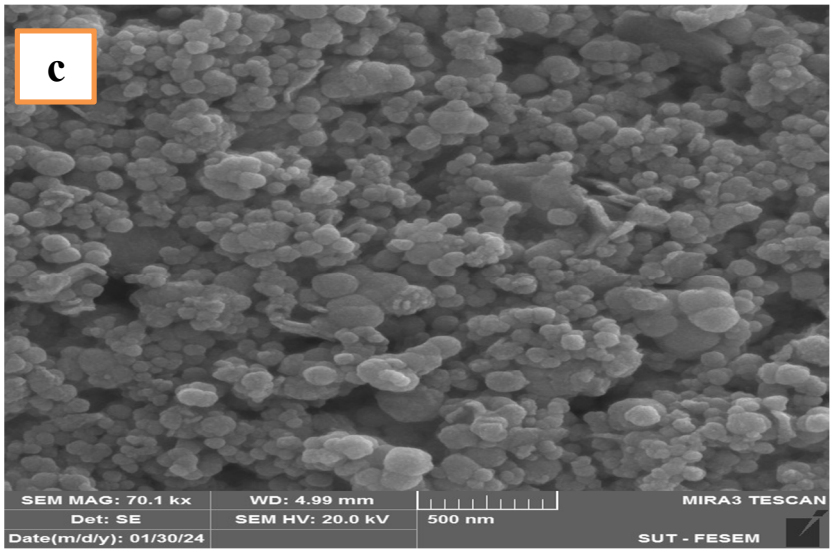

FIG. 2. FESEM surface images of nickel ferrite at different pH levels: a) 5 ph. b) 9 ph. c) 11 ph.

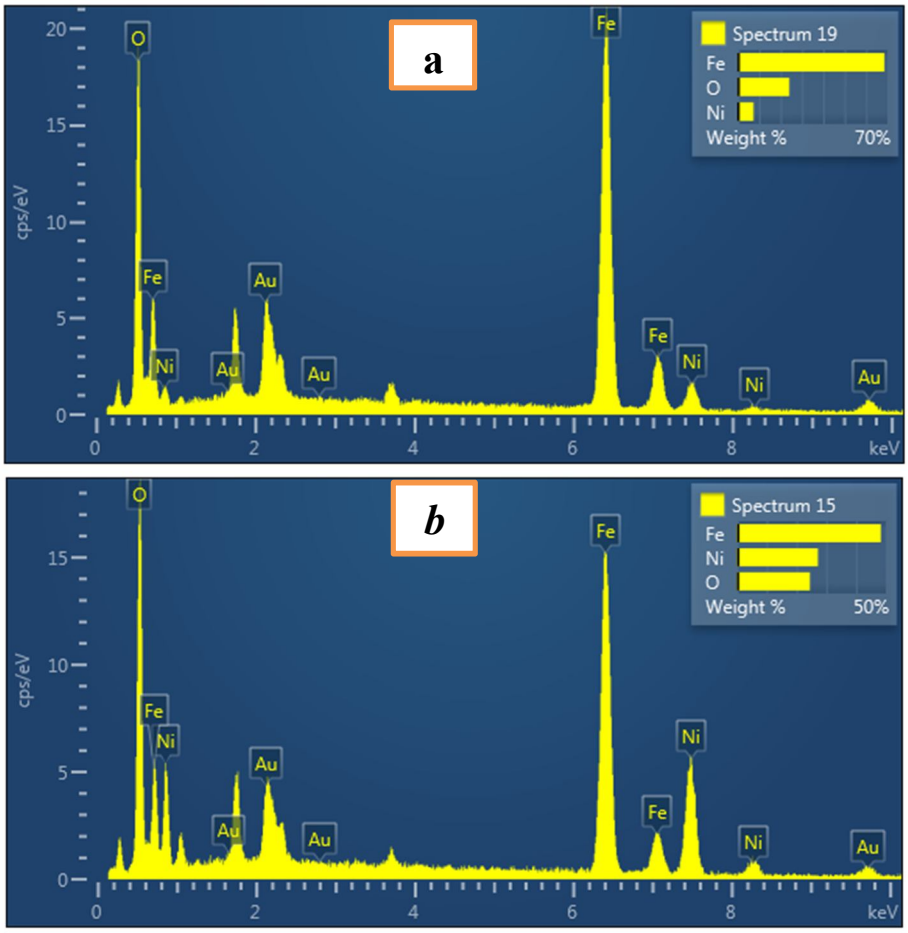

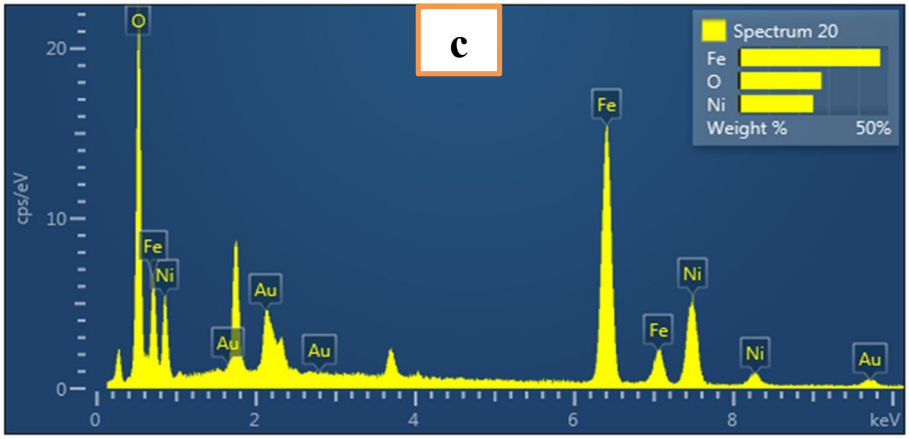

FIG. 3. EDX analysis results for nickel ferrite nanoparticles at different pH levels; a) 5 ph. b) 9 ph. c) 11 ph.

3.4 Vibrating Sample Magnetometer (VSM) Measurements

In this study, the magnetic characteristics of nickel ferrite nanoparticles synthesized at various pH values were examined using the vibrating sample magnetometer (VSM) technique. With numerous applications in science and engineering, VSM analysis is one of the most widely used and precise methods for examining the characteristics of magnetic materials [22]. Hysteresis loop observation suggests that the samples are ferromagnetic in nature. Table 2 displays the saturation magnetization (M_S) and the coercivity (H_{ci}) of prepared samples, which were taken from Fig. 4.

TABLE 2. The values of the coercivity (Hci) and saturation magnetization (Ms) of NiFe2O4 formed at different pH levels.

Sample	M_s (emu/g)	H_{ci} (Oe)
5 PH	1.8	4.1
9 PH	13.7	25.2
11 PH	17.4	30.4

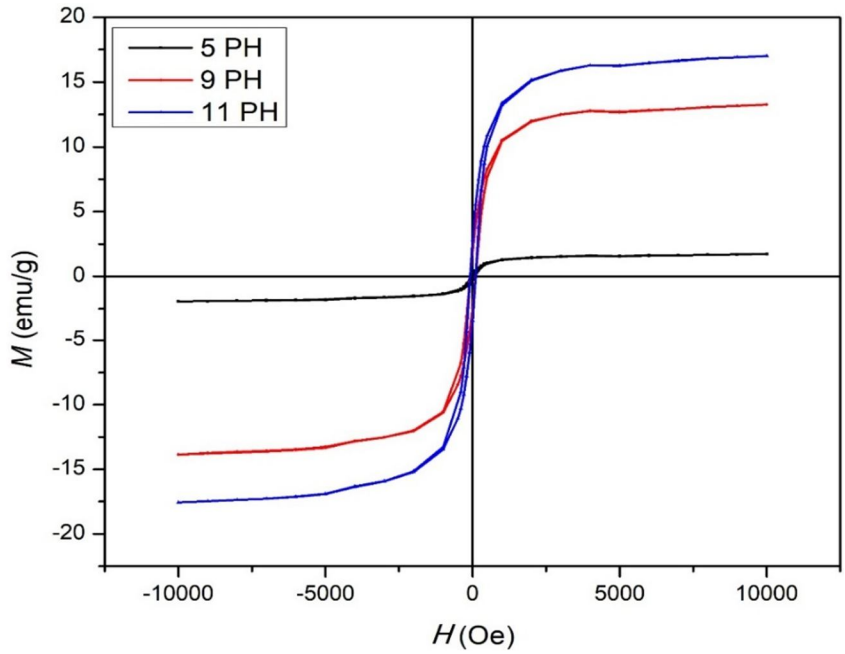

FIG. 4. The magnetization (emu/g) as a function of magnetic field (Oe) of nickel ferrite ($NiFe_2O_4$) nanoparticles formed at different pH levels.

The saturation magnetization values rise with increasing pH, as can be seen in the figure: the sample's values at pH levels of 5, 9, and 11 are 1.8, 13.7, and 17.4 emu/g, respectively. The sample with a pH of 5 displayed extremely low saturation magnetism, primarily due to the purity of the ferrite phase [7]. This result is consistent with the results of X-ray diffraction and FESEM analysis, which confirm that the properties of the material improve with increasing pH. Saturation magnetization varies greatly depending on the ferrite phase's particle size and phase purity; it is lower for smaller particles because of the spin-glass surface layer, and it increases with decreasing particle diameter [7, 22, 23].

3.5 Optical Properties

The pH is a very important factor because it controls the reduction rate for the formation of nanoparticles. The pH values of 5, 9, and 11 were utilized in the preparation of nickel ferrite nanoparticles. The resultant solution's absorbance measured in the 200–700 nm wavelength range using UV–Vis spectroscopy is shown in Fig. 5. The highest absorption peak was recorded at pH 11, which is attributed to an increase in free carriers in the conduction bands and a corresponding rise in the intensity of visible light absorption [17]. The observed blue shift of the absorption peaks toward shorter wavelengths indicates a reduction in particle size as a result of quantum confinement effects in the nanoparticles, accompanied by an increase in the surface-area-to-volume ratio [24]. This observation is consistent with the X-ray diffraction (XRD) analysis and FESEM images, which reveal that the crystallite and particle sizes decrease with increasing pH.

TABLE 3. UV-Vis absorption peaks of ferrite nickel particles synthesized at different pH values.

PH	λ_{max} (nm)	Abs_{max}
5	421	0.87
9	410	0.98
11	390	1.04

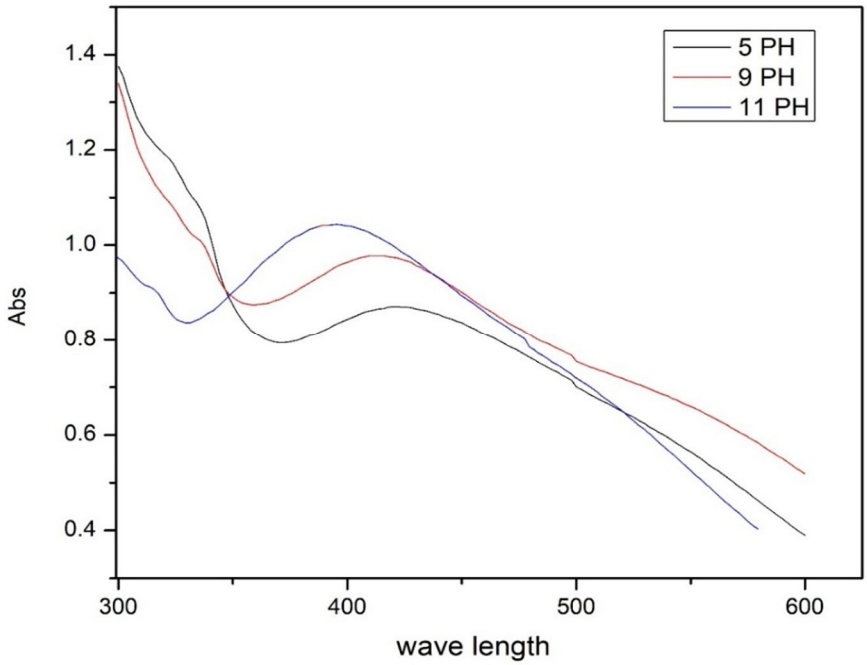

FIG. 5. UV-Vis absorption spectra of nickel ferrite nanoparticles synthesized at different pH levels.

Using the Tauc relation [25, 26], the direct band gap value can be computed from the absorption spectra above.

$$(\alpha hv)^n = B(hv - E_g) \quad (5)$$

Where hv is the photon energy in eV and α is the optical absorption coefficient in cm^{-1}, B is a material-related constant, and n is 2 for direct transitions, such as in $NiFe_2O_4$, which has a direct allowed band gap as demonstrated by [26, 27]. The energy difference between the top of the valence band and the bottom of the conduction band is commonly referred to as the "band gap energy" in solid-state physics for

semiconductors and insulators [28]. The optical band gap of the nickel ferrite nanoparticle samples synthesized at various pH values is displayed in Fig. 6, which illustrates the relationship between the photon energy hv and the square of the optical absorption coefficient α.

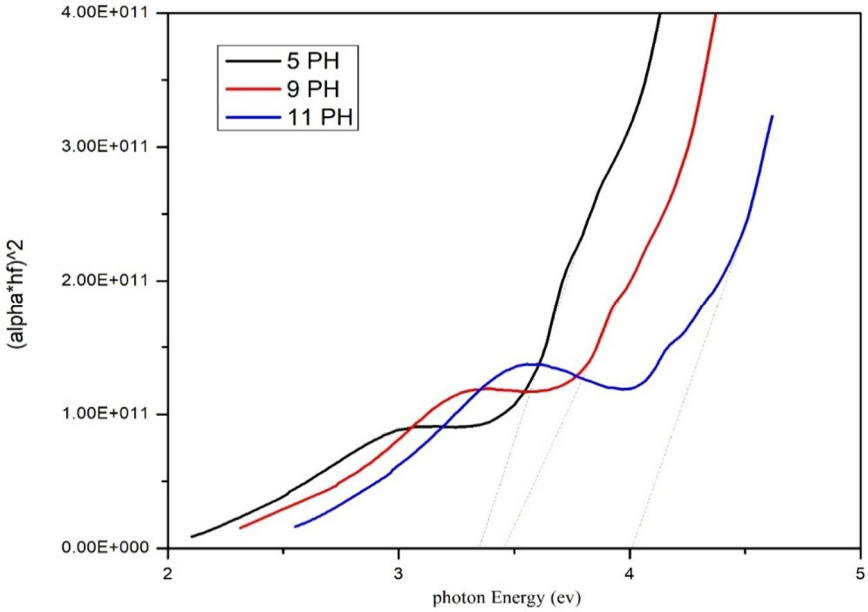

FIG. 6. Band gap spectra for $NiFe_2O_4$ nanoparticles synthesized at different pH levels.

Figure 5 shows that the optical band gap increases from 3.35 to 4.01 eV as the pH value increases from 5 to 11. The increase in the band gap can be attributed to the higher oxygen content in the deposited samples, as confirmed by the EDX analysis. This behavior may also be associated with changes in particle size and crystallinity resulting from variations in the synthesis pH. Changes in the pH factor affect the oxygen content, which directly affects the energy band gap of a certain prepared sample. So it is the increase in the oxygen content that is responsible for the increase in the energy gap. This phenomenon is understood in the context of the role of oxygen atoms as electron acceptors, which increases the energy difference between the top of the valence band and the bottom of the conduction band [29, 30]. To sum up, the variations in the pH level can cause changes in the oxygen content, which in turn can explain the changes in the optical band gap of the nickel ferrite nanoparticles.

3.6 Current – Voltage (I-V) Characteristics

The optical, structural, and magnetic properties of the synthesized nickel ferrite nanoparticles at different pH values were examined in order to determine the ideal pH for preparation and use in photodetector applications. The ideal pH was found to be 11. The current-voltage characteristic is an important parameter in the application of photodetectors, as the current-voltage characteristic curve describes the current generated under forward and reverse bias in dark and light conditions. A schematic of the photo response measurement apparatus and the current-voltage ratio curves of the devices in both light and dark conditions for the sample at pH 11 deposited on n-Si substrates are exhibited in Fig. 7. A light-emitting diode (LED) with a wavelength of 350 nm was used to illuminate the device. Under both forward and reverse bias conditions, the current and voltage exhibit symmetry, suggesting a narrow depletion layer width in the junction [31, 32]. It has been noted that as the applied forward bias voltage rises, so does the current. The width of the depletion region increases with increasing the applied reverse bias voltage, which leads to the separation of electron-hole pairs, at which point the current increases. The incident light causes the generation of a photocurrent resulting from the incident light photons [33, 34].

The forward dark current originates from the flow of majority charge carriers. Under forward bias conditions, the applied voltage injects majority carriers across the junction, resulting in a reduction in the depletion layer width and the built-in potential barrier. In the low voltage region (0-1 V), the current is primarily governed by carrier recombination because the

concentrations of minority and majority carriers exceed the intrinsic carrier concentration ($n^2 < np$). The slight increase in recombination current within this region indicates that electrons are thermally excited from the valence band (VB) to the conduction band (CB), where they subsequently recombine with holes in the valence band.

As the applied voltage increases further, the current rises rapidly due to the dominance of diffusion current mechanisms [35, 36]. In contrast, the reverse-bias current decreases, which may be attributed to the formation of structural defects and dislocations that reduce charge-carrier mobility. These defects can introduce localized energy states within the band gap and act as recombination centers, thereby suppressing carrier transport across the junction. Fig. 7 confirms the Schottky behavior of the fabricated junction.

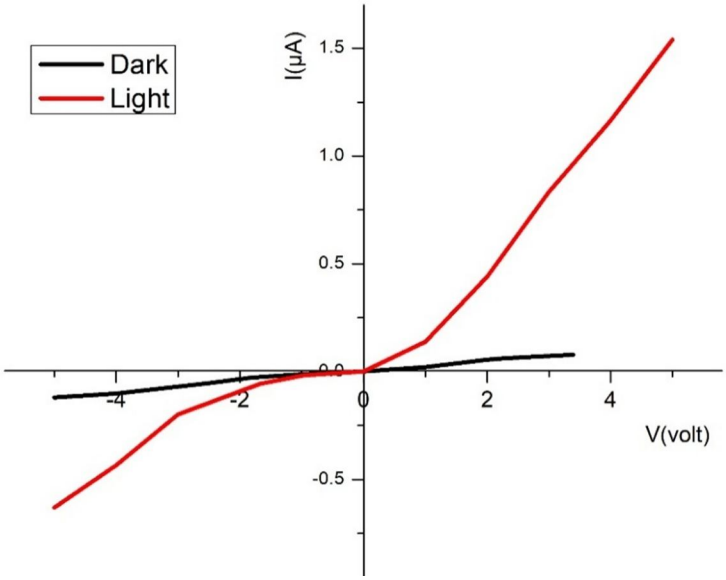

FIG. 7. Current–voltage (I–V) characteristics of nickel ferrite nanoparticles synthesized at pH 11 under dark and illuminated conditions.

3.7 Photosensitivity

The conductivity increases when the light is switched on and returns to its initial level when the light is turned off. As seen in Fig. 8, this process is repeated periodically through successive ON/OFF switching cycles, with each cycle exhibiting characteristic rise and decay times. The current-time (I-t) measurements were recorded under illumination at a wavelength of (350) nm.

Since the photon energy corresponding to 350 nm (~3.55 eV) is lower than the optical band gap energy of the film, the photodetection process is mainly attributed to the excitation of electrons through defect-related energy states within the band gap. The involvement of these defect states in the photodetection mechanism may explain the relatively long rise and decay times observed in the photodetector response.

The photosensitivity of the nickel ferrite nanoparticle photodetector was evaluated using Eq. (6) [29]:

$$S = \frac{I_{PH} - I_d}{I_d} \times 100\% \quad (6)$$

where I_d represents the dark current and I_{PH} denotes the photocurrent. This calculation yielded a sensitivity of 231.89%.

The data indicates that electrons in the nickel ferrite nanoparticles gain excitation energy from the incident light source, enabling reversible switching between low- and high-conductivity states. This reversible behavior allows effective modulation of the current response in the nickel ferrite photodetector. As shown in Fig.8, the rise time from the minimum to maximum current value is approximately 1.6 s, whereas the decay time after witching off the illumination ranges from 1 to 3 s. The illumination cycles were periodically repeated at predetermined intervals.

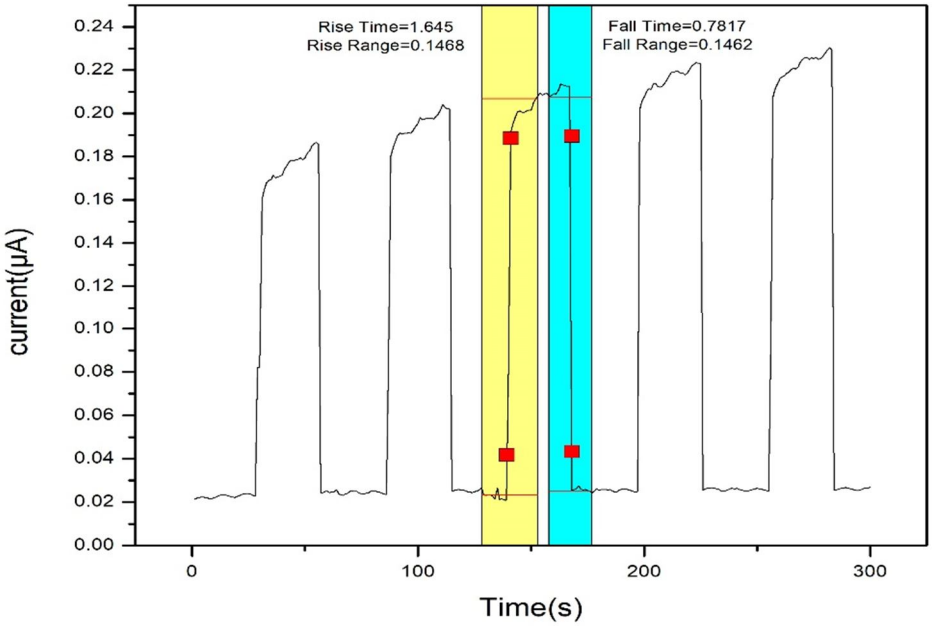

FIG. 8. Nickel ferrite nanoparticle sensitivity and rise and fall times.

3. Conclusion.

Nickel ferrite ($NiFe_2O_4$) nanoparticles were synthesized using the hydrothermal method at different pH values. XRD analysis confirmed the successful formation of $NiFe_2O_4$ nanoparticles with a face-centered cubic (FCC) crystal structure and demonstrated the influence of pH on the crystal structure and crystallite size distribution. FESEM analysis revealed that the synthesized nanoparticles were predominantly spherical in morphology with particle sizes below 100 nm.

UV-Vis spectroscopy showed an increase in the absorption intensity accompanied by a blue shift with increasing pH. EDX spectra clearly confirmed the presence of Fe, Ni, and O in the synthesized $NiFe_2O_4$ nanoparticles. In addition, the saturation magnetization values were found to increase with increasing pH.

This study was further extended to the fabrication of a thin $NiFe_2O_4$ film deposited on silicon wafers for photodetector applications. The fabricated device exhibited a high photosensitivity of 231.89%, demonstrating a rapid and significant photoresponse under illumination at a wavelength of 350 nm.

References

[1] Hajia, B.S. and Barzinjy, A.A., Jordan Journal of Physics, 15 (5) (2022) 429.

[2] Malik, S., Muhammad, K., and Waheed, Y., Molecules, 28 (2) (2023) 661.

[3] Lambat, T.L., Ledade, P.V., Gunjate, J.K., Bahekar, V.R., Mahmood, S.H., and Banerjee, S., Results in Chemistry, 6 (2023) 101176.

[4] Al-Sharif, A. and Abo-AlSondos, M., Jordan Journal of Physics, 1 (2) (2008) 61.

[5] Bopche, Y.S., Shahare, A.M., Bagde, A.V., and Choudhary, D.S., Jordan Journal of Physics, 15 (1) (2022) 61.

[6] Rana, G., Dhiman, P., Kumar, A., Vo, D.-V.N., Sharma, G., Sharma, S., and Naushad, M., Chemical Engineering Research and Design, 175 (2021) 182.

[7] Al-Hunaiti, A., Ghazzy, A., Sweidan, N., Mohaidat, Q., Bsoul, I, Mahmood, S., and Hussein, T., Nanomaterials (Basel), 11 (4) (2021) 1010.

[8] Patel, G., Patel, A.R., Lambat, T.L., Mahmood, S.H., and Banerjee, S., FlatChem, 21 (2020) 100163.

[9] Yang, G. and Park, S.J., Materials (Basel), 12 (7) (2019) 1177.

[10] Mustafa, A., Turki Al-Rashid, S.T., Chalcogenide Letters, 21 (5) 407.

[11] Aneesh Kumar, K.S., Bhowmik, R.N., and Mahmood, S.H., Journal of Magnetism and Magnetic Materials, 406 (2016) 60.

[12] Nejati, K. and Zabihi, R., Chemistry Central Journal, 6 (2012) 23.

[13] Al-Hunaiti, A., Mohaidat, Q., Bsoul, I., Mahmood, S., Taher, D., and Hussein, T., Catalysts, 10 (2020) 839.

[14] Mamdooh, N.W., Ibrahim, I.M., and Al Rashid, S.N.T., 6th International Conference for Physics and Advance Computation Science AIP Conference Proceedings, 3282, 050042-1-050042-9.

[15] Samson, V.A., Bernadsha, S.B., Xavier, R., Rueshwin, C.S.T., Prathap, S., Madhavan, J., and Raj, M.V.A., Materials Today: Proceedings, 50 (7) (2022) 2665.

[16] Shlapa, Y., Solopan, S., Sarnatskaya, V., Siposova, K., Garcarova, I., Veltruska, K., and Timashkov, I., Colloids and Surfaces B: Biointerfaces, 220 (2022) 112960.

[17] Mamdooh, N.W. and Naeem, G.A., AIP Conference Proceedings, 2450 (1) (2022) 020045.

[18] Calvache-Muñoz, J., Prado, F.A., and Rodríguez-Páez, J.E., Colloids and Surfaces A:Physicochemical and Engineering Aspects, 529 (2017) 146.

[19] Al-Gebory, L. and Mengüç, M.P., Journal of Quantitative Spectroscopy and Radiative Transfer, 219 (2018) 46.

[20] Udhaya, P.A., Meena, M., Queen, M.A.J., Freeda, M.M., and Das, T.R., Jordan Journal of Physics, 14 (2021) 437.

[21] Nasrollahzadeh, M., Atarod, M., Sajjadi, M., Sajadi, S.M., and Issaabadi, Z., "Plant-Mediated Green Synthesis of Nanostructures: Mechanisms, Characterization, and Applications", In: "Interface Science and Technology", Elsevier, 28 (2019) 199.

[22] Gopale, S., Kakade, G., Kulkarni, G., Vinayak, V., Jadhav, S., and Jadhav, K.M., Journal of Physics: Conference Series, 1644 (2020) 012010.

[23] Elashmawi, I.S. and Ismail, A.M., Polymer Bulletin, 80 (2022) 2329.

[24] Kaliva, M. and Vamvakaki, M., Materials Science and Technology, 2020 (2020) 401.

[25] Hameed, A.A., Mohammed, J.F., and Ibrahim, I.M., 6th International Conference for Physics and Advance Computation Sciences, 3282.

[26] Ahmad, N., Alam, M., Ansari, A., Alrayes, B., Ahmed, M., and Alotaibi, M., Nanoscience and Nanotechnology Letters, 9 (2017) 1688.

[27] Babu Naidu, K.C. and Madhuri, W., Bull. Materials Science, 40 (2017) 417.

[28] Mohapatra, S. and Nguyen, T.A., "Phuong Nguyen-Tri", In: "Micro and Nano Technologies, Noble Metal-Metal Oxide Hybrid Nanoparticles", (Woodhead Publishing, 2019), 645-659.

[29] Hathal, Y.R., Ibrahim, I.M., and Khalaf, M.K., Iraqi Journal of Applied Physics, 20 (2B) (2024) 349.

[30] Alrashid, S., Nanoscience and Technology, 15 (2024) 21.

[31] Hamdan, S.A., Ibrahim, M., and Ali, I.M., Journal of Physics: Conference Series, 2114 (2021) 012025.

[32] Das, M., Middya, S., Datta, J., Dey, A., Jana, R., Layek, A., and Ray, P., Journal of Electronic Materials, 45 (8) (2016) 4293.

[33] Hameed, A.A., Ibrahim, I.M., and Mohammad, J.F., Journal of Optics 2025 (2025).

[34] Mazhir, S.N. and Abbas, H.H., Baghdad Science Journal, 21 (5) (2024) 1684.

[35] Abbas, N.K., Ibrahim, I.M., and Saleh, M.A., Silicon, 10 (2018) 1345.

[36] Hamdan, S.A. and Ali, I.M., Iraqi Journal of Physics, 17 (40) (2019) 77.